information services
gwasanaethau gwybodaeth

1 # Unraveling Structure Sensitivity in CO_2 Hydrogenation over Ni

2 Charlotte Vogt[†], Esther Groeneveld[‡], Gerda Kamsma[‡], Maarten Nachtegaal[§], Li Lu[¥], Christopher J.

3 Kiely[¥], Peter H. Berben[‡], Florian Meirer[†], Bert M. Weckhuysen[†,*]

4 [†]Inorganic Chemistry and Catalysis group, Debye Institute for Nanomaterials Science, Utrecht University, Universiteitsweg

5 99, 3584 CG Utrecht, the Netherlands

6 [‡] BASF Nederland B.V., Strijkviertel 61, 3454 PK De Meern, the Netherlands

7 [§] Paul Scherrer Institute (PSI), 5232 Villigen PSI, Switzerland

8 [¥]Department of Materials Science and Engineering, Lehigh University, 5 East Packer Avenue, Bethlehem, PA 18015, USA

9 *B.M.Weckhuysen@uu.nl

10

11

12

13
14
15 ABSTRACT (100-150 words): Continuous efforts in the field of materials science have allowed us to generate smaller and

16 smaller metal nanoparticles, creating new opportunities to understand catalytic properties that depend on the metal particle

17 size. Structure sensitivity is the phenomenon where not all surface atoms in a supported metal catalyst have the same activity.

18 Understanding of it can assist in the rational design of catalysts allowing control over mechanisms, activity and selectivity,

19 and thus even the viability of a catalytic reaction. Using a unique set of well-defined silica-supported Ni nanoclusters (1-7

20 nm) and advanced characterization methods, we prove how structure sensitivity influences the mechanism of catalytic CO_2

21 reduction, the nature of which has been long debated. These findings bring fundamental new understanding of CO_2

22 hydrogenation over Ni and allow us to control both activity and selectivity, which can be a means for CO_2 emission

23 abatement through its valorization as a low, or even negative cost feedstock, on a low-cost transition metal catalyst.

The reduction of CO_2 emissions into the earth's atmosphere is gaining legislative importance in view of its impact on the climate[1–5]. Reduction of the harmful effect of these emissions through reclamation of CO_2 is made attractive because CO_2 can be a zero- or even negative-cost carbon feedstock[6,7]. The conversion of renewably produced hydrogen and CO_2 into methane, or synthetic natural gas (SNG), over Ni is a solution which combines the potential to reduce CO_2 emissions, with a direct answer to the temporal mismatch in renewable electricity production capacity and demand[8–17]. Chemical energy storage in the form of hydrogen production by electrolysis is a relatively mature technology, however the required costly infrastructure, and inefficiencies in distribution and storage deem it inconvenient for large-scale application in the near future. Point source CO_2 hydrogenation to methane yields an alternative with higher energy density. Furthermore, methane is more easily liquefied and can be stored safely in large quantities through infrastructures that already exist[18,19].

The search for fossil fuel alternatives, and application of a process such as that described above can arguably only be achieved with the help of advances in catalysis and the closely related field of nanomaterials. Continuous efforts in both fields have allowed us to make increasingly smaller and catalytically more active (metal) particles. However, it is already known that making infinitesimally smaller supported catalyst particles doesn't necessarily linearly correspond to higher catalytic activity[20–22]. This phenomenon, where not all atoms in a supported metal catalysts have the same activity, is called structure sensitivity and is often attributed to the distinctly different chemistries on different lattice planes for π-bond activation in CO_2, or σ-bond activation in H_2 dissociation and C-H propagation[20,23]. The availability of stepped (less coordinated) versus terrace (more coordinated) sites on the surface of supported catalyst nanoparticles obviously changes with particle size, and atomic geometries become particularly interesting below 2 nm where for example π-bond activation is believed to not be able to occur[20]. While particle size effects have extensively been studied for CO hydrogenation over Co[22,24], understanding of structure sensitivity effects of these critical particle sizes are lacking as sub 2 nm particles prove difficult to synthesize for first row transition metals (Co, Fe and Ni). In this work we used a unique set of SiO_2-supported Ni nanoparticles with diameters ranging from 1-7 nm in size, and show not only the existence of a distinct particle size effect, but also evidence that allows us tounderstand the structure-sensitivity of CO_2 hydrogenation over Ni as a model structure sensitive reaction.

Classically, CO_2 hydrogenation over nickel is considered to follow a 2-step, Langmuir-Hinshelwood type mechanism whereby first CO_2 dissociatively adsorbs with H_2 to form CO and H_2O in the reverse water gas shift (RWGS) reaction. The CO is then subsequently directly hydrogenated or dissociates to atomic C_{ads} and is then hydrogenated as schematically depicted in Figure 1[6,7]. However, recent experimental and theoretical studies show that this reaction mechanism, particularly on surfaces of non-model catalysts, is not fully understood[25–30]. The reverse water gas shift reaction is believed to follow either of two mechanisms: firstly, a surface carbonate to formate reaction pathway (pathway 1 in Figure 1), and secondly, the

2

direct dissociation of CO_2 to CO via a CO_2^- ion (pathway 2 in Figure 1). Much of the debate in the literature arises from the direct comparison between model and non-model surface studies. We hypothesize that mechanistic understanding of this reaction is closely related to its structures sensitivity.

Enhanced understanding of structure sensitivity and mechanistic aspects behind this reaction will not only be a step towards a feasible method for the valorization of CO_2, with the potential to reduce its impact on the environment, but it will also aid in understanding similar structure sensitive reactions. Evidence for the impact of different atomic coordinations in metal nanoclusters on the activation of different bond-types, however, can have far greater, multidisciplinary impact as it will allow the rational design of catalysts enabling us to control, at the atomic level, the activity and selectivity of catalytic reactions[31–33]. It may even facilitate the discovery of new, previously unattainable catalytic reactions.

1
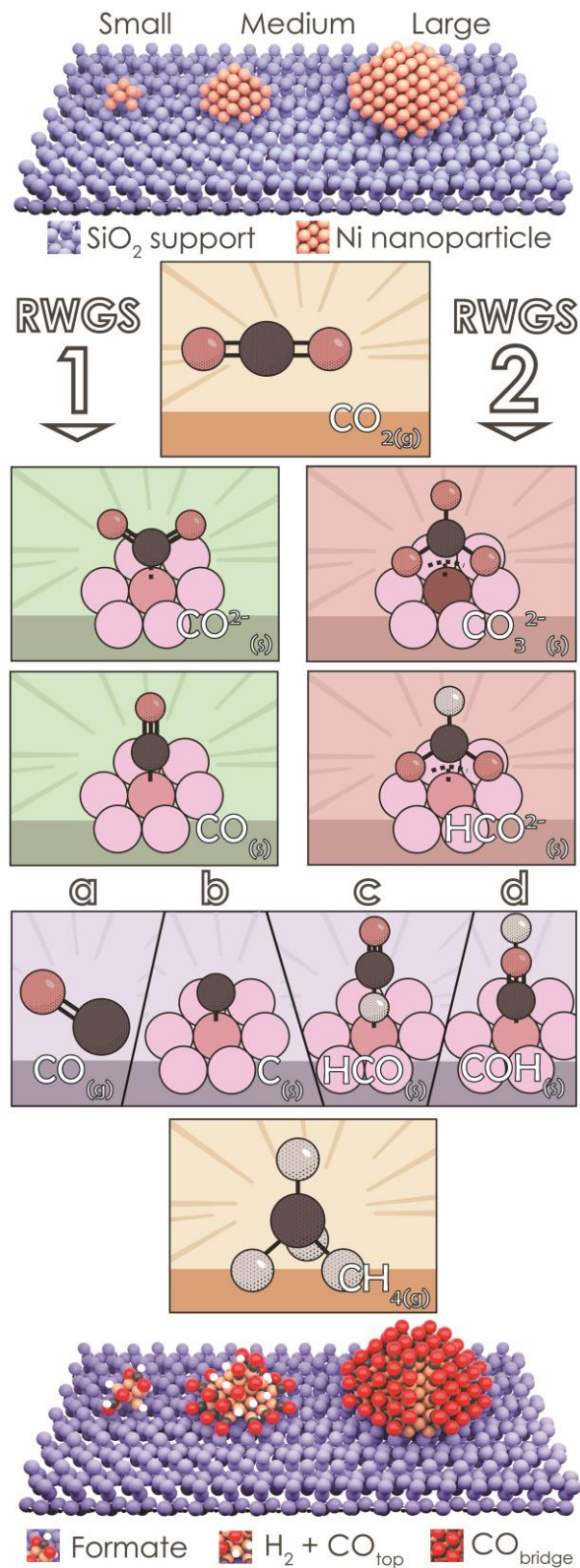
Figure 1| Mechanisms of catalytic CO$_2$ hydrogenation. Schematic overview of the mechanisms behind CO$_2$ hydrogenation as currently proposed in literature, with simplification of certain non-rate determining steps (RDS) following the purple panels. Pathway 1 and 2, preceding green and red boxes, indicate reverse-water-gas-shift (RWGS) mechanisms, in which a darker colored atom in the cluster represents the higher oxidation state of Ni resulting from each step. The depiction is simplified to merely top-adsorption but it is important to ascertain the coordination of Ni sites in each reaction step.

4

RESULTS

OPERANDO FT-IR SHOWS TWO SEPARATE, PARTICLE SIZE DEPENDENT RWGS MECHANISMS.

3   A set of well-defined SiO_2 supported Ni catalysts was prepared by deposition precipitation resulting in different nanoparticle

4   sizes, ranging from 1-7 nm, by varying the weight loading of the precursor solutions. Particle sizes and oxidation states of

5   fresh, reduced and spent catalysts were characterized by multiple techniques as summarized in Table 1; details concerning

6   the characterization can be found in the Supplementary Information (see sections 'Methods' and 'Characterization Results',

7   Figures S1-S6). The catalysts with different particle sizes were systematically tested in an operando transmission FT-IR

8   spectroscopy set-up, while recording on-line activity data. Figure 2 shows the observed activities towards methane formation

9   in CO_2 hydrogenation with a 4:1 ratio of H_2:CO_2 at ambient pressure. Change in nanocluster size during catalytic reaction

10   was not significant, as evidenced by post reduction and spent structural characterization listed in Table 1. The turnover

11   frequency (TOF) and activity (Figure 2b and 2c) were determined at 400 °C, and using particle sizes after reduction, as

12   determined by HAADF-STEM. Several additional trends serving to underwrite the attributed particle size effects to surface

13   specific activity are reported in the Supplementary Information (see section 'Particle Size vs. Activity Relationships', Figures

14   S7-S9). In contrast to the extensively studied CO hydrogenation over Co (Fischer-Tropsch synthesis), where the TOF does

15   not change for particle sizes larger than 6 nm[22,24], we observed a maximum activity at around 2.5 nm for CO_2 hydrogenation

16   over Ni at 400 °C (Figure 2b). We have thus established a particle size effect by use of a unique set of well-defined catalyst

17   samples, that is, the surface specific activity of catalytic CO_2 hydrogenation over Ni changes with Ni particle size.
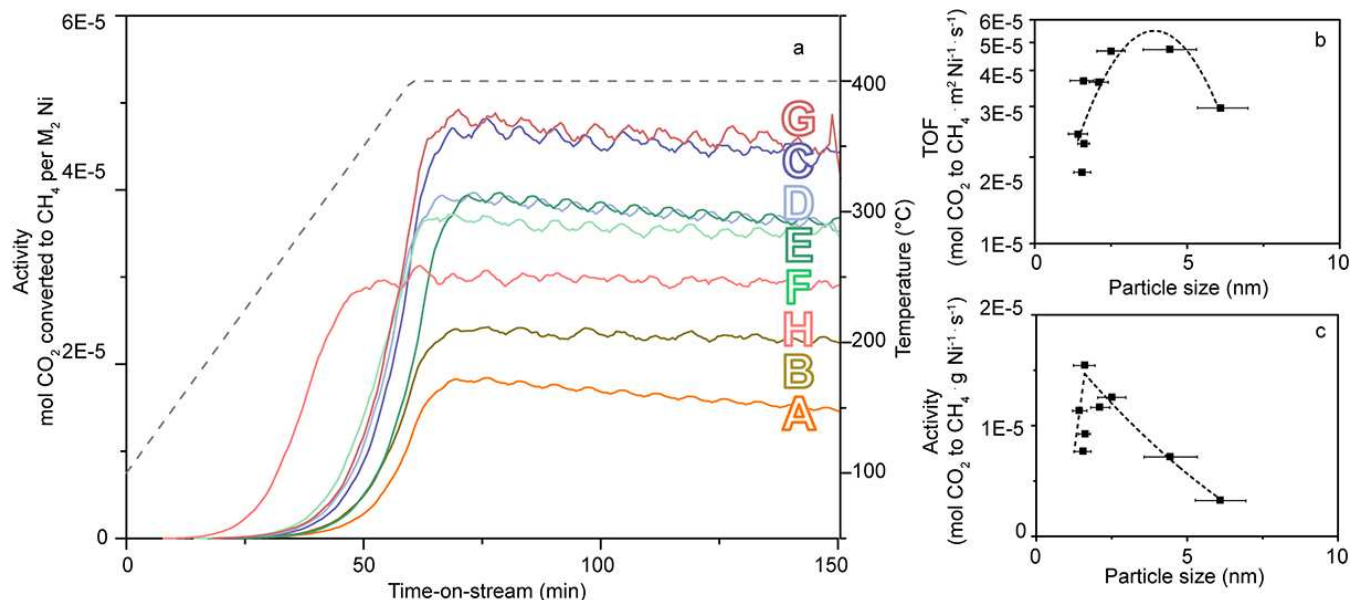
18

Figure 2| a, Methane activity profiles normalized to Ni surface area in m² (assuming hemispherical particles) for catalyst samples A-H (see table 1) the dotted grey line denotes the temperature profile, $H_2/CO_2 = 4$, 1 bar. **b,** The influence of Ni particle size on the TOF in grey (400 °C, $H_2/CO_2 = 4$, 1 bar). **c,** The influence of Ni particle size on activity normalized to the Ni loading (400 °C, $H_2/CO_2 = 4$, 1 bar).

1

2   Operando spectroscopy was employed to relate these particle size, or structure sensitivity effects to surface species and

3   processes. In Figures 3a and 3b, difference FT-IR spectra are shown, i.e. where the first spectrum of the series is subtracted

4   from subsequent spectra. These consecutive spectra are focused on the absorption region between 2250-1400 cm^{-1}, where

5   amongst other things intermediate C≡O to C-O stretching vibrations occur[34–37]. Furthermore we also observe C-H stretching

6   vibrations at 3015 cm^{-1} for methane (Figure 3c), and peaks at 1932, 1866, and 1635 cm^{-1} for framework silica. All spectra

7   were normalized to Ni surface area, and thus contain more intense silica peaks with lower Ni wt%, as can be seen in Figure

8   3a and 3b.

9   Three important reaction intermediates were observed with this type of analysis (Figures 3d-f). Firstly, CO$_{ads}$ with peaks

10   between 2060-1900 cm^{-1} where a distinction can be made between a set of peaks at 2060 cm^{-1} with a shoulder at 2019 cm^{-1},

11   and a peak at 1903 cm^{-1} (Figure 3e, and Supplementary Fig. 10f-h). The former set describes terminally adsorbed CO atop a

12   single Ni atom, and vibrations occur anywhere between 2060-2019 cm^{-1} depending on the oxidation state of Ni[34–37]. The

13   band at 1903 cm^{-1} is ascribed to bridged carbonyl species; more specifically a CO species bound to three neighboring Ni

14   atoms. The second important reaction intermediate is gaseous CO which gives a symmetrical broad band with maxima at

15   2180 cm^{-1} and 2095 cm^{-1} (Figure 3d). Thirdly, a peak around 1591 cm^{-1} is attributed the third intermediate, namely surface

16   formate (Figure 3f, see also section 'FT-IR Studies of Catalyst Samples' of the Supplementary information). We show

17   therefore that intermediates from RWGS pathway 1, as well as pathway 2 in Figure 1, are both present on supported Ni

catalysts. Figure 3a also already clearly shows that the catalyst with the highest Ni dispersion shows relatively few bands in the CO_{ads} region, whereas for the catalyst with the largest Ni nanoparticles (Figure 3b), the peaks in this region are more pronounced. This intriguing trend evolves progressively with increasing particle size, as shown in the Supplementary information (see section 'FT-IR Studies of Catalyst Samples', Figures S10-S12), suggesting that with increasing particle size pathway 1 becomes more dominant.

To assess the evolution of the FT-IR peaks during reaction, Figure 3g shows integrated peak areas plotted against time-on-stream. Here it becomes evident that the intensity of the absorption bands in the CO_{ads} stretching region during CO_2 hydrogenation is positively correlated with, and therefore even an indirect measure for, catalyst particle size. Interestingly, the amount of gaseous CO seems negatively correlated with particle size and is only observed for the smallest particles under investigation (<1.5 nm), i.e., which show lower TOF values. Furthermore, with the knowledge that CO_{ads} atop a single nickel atom (2060-2019 cm^{-1}) has a weaker Ni-C bond than CO adsorbed in a trifold bridge position (1903 cm^{-1}), these FT-IR results also give a first indication of the particle size dependence of Sabatier's general principle for catalysis, where intermediate adsorption strength (in this case of CO), is required for optimal catalyst activity, which is achieved here by Ni particle sizes with diameters in the 2-3 nm range. To corroborate this observation the catalysts were flushed post reaction. As Figure 3h shows, any CO species on the small Ni particle sizes are easily flushed off, while for the large Ni particles the CO_{ads} is indeed present in a much more stable configuration, such as a bridged carbonyl, or carboxylate species.

While both RWGS pathways from Figure 1 seem to occur, as both formate and $CO_{(ads)}$ species are observed in FT-IR, the intermediate species for each pathway show very different adsorption properties for the different particles sizes. Figure 3c shows that formate species are present irrespective of catalyst particle size, however for the smaller Ni particle sizes, we see no decrease of the band during reaction as we do for larger Ni particle sizes. To assess whether both formate and CO species are still reactive, isotopically labelled gas feedstocks ($^{13}CO_2$, and D_2) were introduced. Interestingly, when pulsed with these labelled feedstocks, no interplay is observed between adsorbed ^{12}C, and H in the formate species and the isotopically labelled feedstocks for small Ni particle sizes. For the larger Ni particle sizes these labelled gases readily interacted and shifted the formate peak with both D_2 and $^{13}CO_2$ pulses at any given point in the reaction (Figure 3i). Whereas for the larger Ni nanoparticles intermediate CO_{ads} species dominate the surface, in the case of the smaller metal nanoparticle sizes formate species dominate and gaseous CO is also observed. These findings are crucial for developing a mechanistic understanding of our observed structure sensitivity effects.
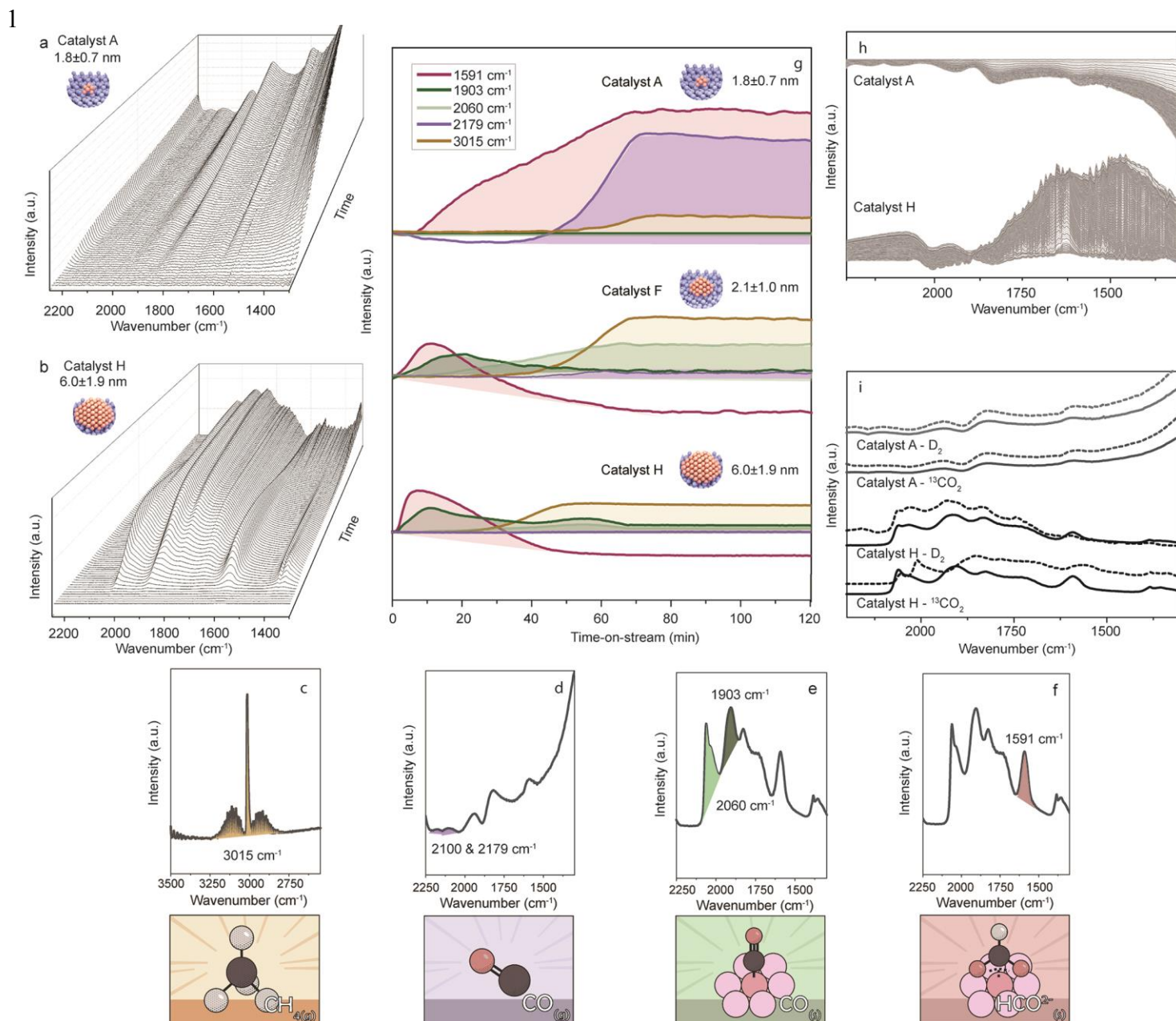
1

Figure 3| Combined operando FT-IR and catalyst activity measurements a, b, Consecutive FT-IR spectra of the CO stretching absorption region plotted against time-on-stream for catalyst A and catalyst H, respectively. At 2060 cm⁻¹, C=O stretching vibration are observed, ascribed to linearly/terminally adsorbed CO atop a single Ni atom. At 2030 cm⁻¹ C=O stretching vibrations can be seen ascribed to linearly/terminally adsorbed CO atop a single Ni(II) or Ni(III) atom. The peak at 1918 cm⁻¹ is attributed to bridged or 3-fold carbonyl C=O stretching vibrations, existing only for the larger particle sizes but convoluted with SiO_2 framework stretching. The band at 1847 cm⁻¹ shows SiO_2 framework stretching vibration peaks, and the one at 1591 cm⁻¹ shows conjugated C-O/C=O stretching vibration from formate species.[34–37,47–50]. **c-f,** FT-IR spectra with highlighted peak areas for methane, gaseous CO, adsorbed CO, and formate species. **g,** Integrated FT-IR peak areas as a function of time-on-stream. **h,** Consecutive operando FT-IR spectra recorded during post-reaction flushing with N_2 of the catalyst with the highest (Catalyst A), and the lowest dispersion (Catalyst H). **i,** Operando FT-IR spectra recorded during CO_2 hydrogenation experiments pulsed with labeled feedstocks. Solid lines denote non-pulsed feedstock, while a dotted line denotes a subsequent pulse of either $^{13}CO_2$, or D_2.

QUICK-XAS EXPLAINS OBSERVED STRUCTURE SENSITIVITY EFFECTS. To further investigate the origin of the observed structure sensitivity effects described above we applied operando quick X-ray absorption spectroscopy (Q-XAS) with an effective time resolution of 4 s. To this end, 100 s CO_2 and H_2 gas pulses were alternated by 30 s N_2 pulses over the catalysts at 400, 350 and 300 °C. These measurements were performed for the two smallest catalyst particle sizes (A and B, 1.4-1.8 nm, 1% and 5% Ni loading respectively), and a sample with slightly larger Ni particle size (F, 2-3 nm, 11.8% Ni loading). Samples A, B, and F were chosen because they showed sufficient X-ray absorption (i.e. Ni weight loading), and because the particles on the catalysts were predominantly below 3 nm which theoretically ensures >35% surface atoms and thus sufficient signal in bulk Q-XAS to detect surface changes[38,39]. Section 'Operando quick-XAS' of the Supplementary information describes in detail the clustering and least squares fitting approach we applied, which resulted in a quantitative value of Ni metal relative to NiO. The percentage of metallic nickel is plotted in Figure 4, showing its evolution with time-on-stream.

The results of this operando spectroscopic characterization analysis are striking and it is worth highlighting that these experiments show exceptional sensitivity, as we are able to detect subtle surface oxidation state changes. Firstly, without using a priori knowledge we were able to distinguish the gas-flow pulse switches between feedstocks (CO_2 and H_2) in the oxidation state of the nickel. It is highly interesting that this method is thus sensitive to 1-2% changes in oxidation state. A second striking observation is that for all Ni particle sizes, the initial oxidation process is direct, but a second slope initiates at the same degree of metallic Ni that the subsequent H_2 pulses re-reduce to. This indicates that on each particle, there are slower and faster mechanisms for CO_2 activation which occur at different catalytic sites. Furthermore, for larger Ni particles there is a two-step re-oxidation (evidenced by a plateau in the plot in Figure 4) for subsequent CO_2 pulses indicating that, either with H_2 or with CO_{ads} on specific sites, a second, less preferred mechanism takes place for the RWGS reaction on larger particles that is slower and in which Ni has a higher overall oxidation state as in for example less active pathway 2 in Figure 1 where Ni with a higher oxidation state is inevitably formed. This plateau is much less apparent for catalysts with smaller Ni particle sizes, with even less terrace sites. These results are in line with the assignment of more coordinatively saturated sites to the less active RWGS pathway 2 in Figure 1. The initial oxidation observed during the N_2 pulse is likely to be caused by a residue of CO_2 in the valve and the lines after switching (see section 'Operando Quick-XAS' in the Supporting information). For the smaller metal nanoparticles, it is clear that the removal of oxygen or charged intermediates such as formate (as we know from FT-IR), is hampering activity, again underwriting that the formate pathway (pathway 2 in Figure 1) is not the active pathway in RWGS and CO_2 hydrogenation.

The maximum change in degree of reduction for catalyst A is 2.3% (from 97.7 to 95.4%), for catalyst sample B 1.5% (from 96.6 to 95.1%), and for catalyst sample F also 1.5% (from 99.5 to 98.0%). The order of magnitude of these surface changes is important to evaluate as it relates to the order of magnitude of sites that are active in CO_2 activation. According to Figure S20 and section 'Quantification of active sites' of the Supplementary information, a 1.4 nm particle should consist of around 192 Ni atoms, of which approximately 80% are forming the surface. If all of these 153 surface atoms were active purely in CO_2 activation during a pulse of CO_2, half the surface atoms (~77 atoms) would be oxidized while the other half would be covered in CO_{ads}. A change in the reduction degree in the order of 1.5% corresponds to 3 atoms that are changing oxidation state, which means that around 4% of the surface atoms that can be oxidized (~77 atoms) actually oxidizes. Applying this same procedure to catalyst A and F, gives us 7% and 6%, resp. atoms that are active in CO_2 activation, or atoms that are part of active atomic coordinations in these particles. Considering these particle sizes are believed even not to be able to activate π-bonds shows novel insights into what are likely restructuring effects in catalysts with such small particle sizes, as we prove the atomic coordinations that can cleave π-bonds are present (albeit in small quantities) under working conditions.
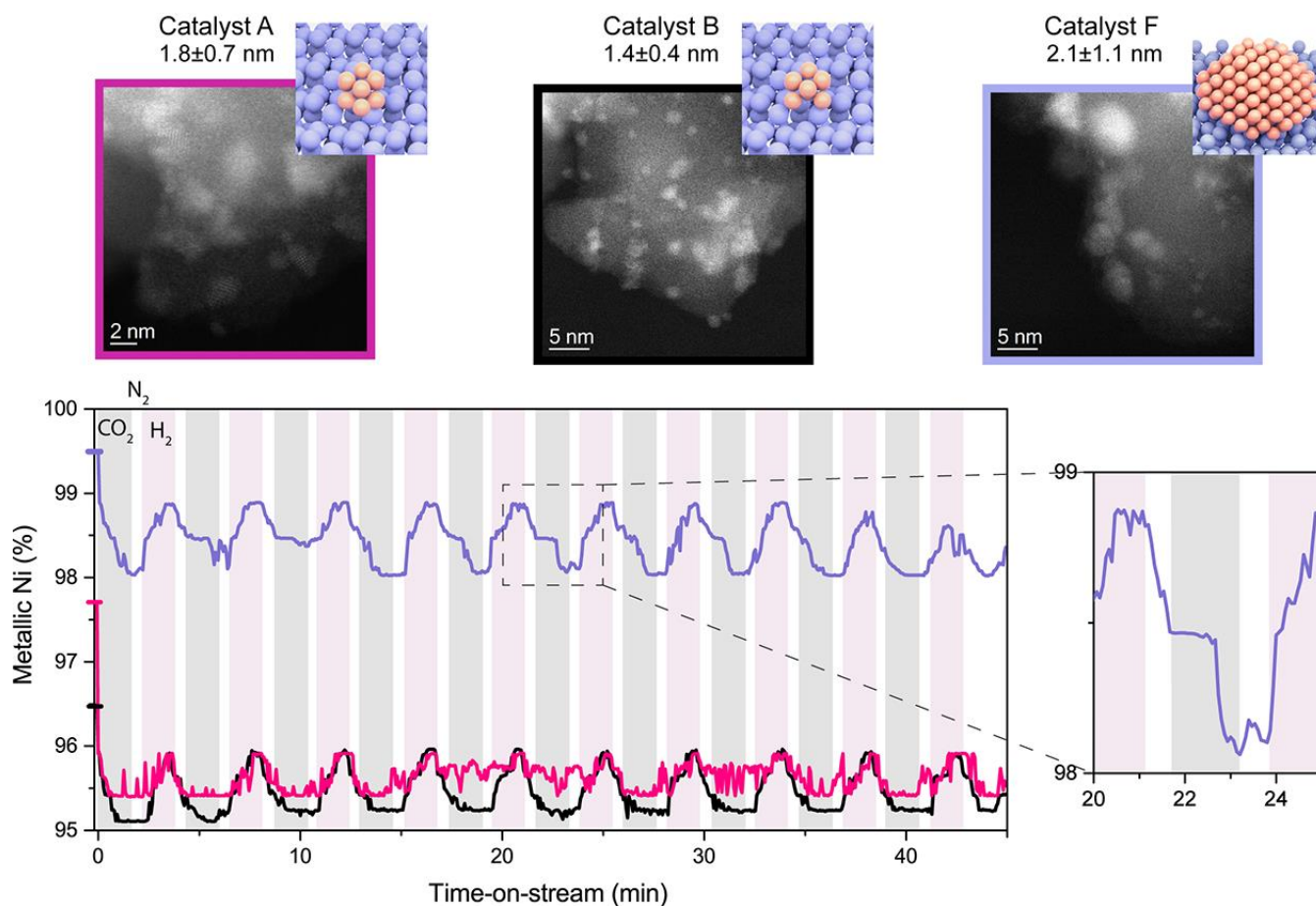

Figure 4| Quick X-ray absorption spectroscopy of three Ni/SiO₂ catalysts with different mean Ni particle sizes. Q-XAS allowed to determine the percentage of metallic nickel with time-on-stream for different nickel nanoparticle sizes; smaller samples A and B (pink and black resp.), and larger particle size sample F (purple) see Table 1 for characterization summary.

DISCUSSION

Operando FT-IR spectroscopy measurements showed that the larger Ni particle sizes retain several types of CO species with high surface coverage, while no gaseous CO is observed. The intensity of peaks in the CO_{ads} stretching region (2060-1600 cm^{-1}) is a measure for Ni particle size. For the catalysts with high Ni dispersion, gaseous CO was observed, along with fewer adsorbed CO species. Clearly, the (re)activity, or stability of intermediate CO plays an important role in the observed Ni particle size effects. Drawing back to the first chemist who described the hydrogenation of CO_2, at first glance Sabatiers principle describes the CO intermediate effects we observe with FT-IR[6,7]. That is, the interactions between the catalyst and the substrate (CO_{ads}) should be just right, neither too strong, nor too weak. In essence, the larger Ni particles under observation are poisoned by a monolayer of CO_{ads} in more stable bridge conformation, while the smallest Ni particles bind CO_{ads} too weakly, facilitating easy desorption. Catalysts facilitating the largest relative amount of linearly adsorbed CO, show the highest activity. Thus the rate-determining step in CO_2 hydrogenation is not the activation of CO_2 or the dissociation of CO, but rather relates to how easily the adsorbed intermediate CO species can be hydrogenated and the availability of adjacent H_{ads} sites to hydrogenate CO_{ads}. In theory this activity should increase with smaller Ni particle size, however this increased activity is likely hampered by the slow removal of oxidizing, or charged surface species in smaller nanoclusters, as shown by Q-XAS. By examining oxidation state changes with high time resolution XAS, complementing the results from operando FT-IR we have identified the influence of more localized energy levels in the electronic band structure of smaller Ni nanoclusters ensuring increased stability of oxidizing or charged species. It is important to note here that it was previously suggested that particles smaller than 2 nm would not be able to cleave π-bonds, while we show experimentally that this is in fact not the case, as we observe gaseous CO and methane even with the smallest Ni particles[20]. These results allow us to discuss the mechanisms portrayed in Figure 1, and point towards the direct dissociation of CO_2 (pathway 1) as the major active pathway in RWGS over Ni at 400 °C.

We are able to identify 3 probable contributions to the structure sensitivity of methanation over Ni catalysts: first, we show operando evidence for the presence of different sites with different activities within a narrow particle size distribution. Second, we show that restructuring likely occurs, at the least for particles <2 nm, to form sites that are active in CO_2 hydrogenation. Finally, we present evidence suggesting that for sub-2 nm Ni particles the lower d-band energy, or higher electron localization has great impact on catalytic activity due to the increased stability of oxidizing or charged species on the surface.

We thus prove that structure sensitivity effects are present in real catalysts and depend on a multitude of physical phenomena. Furthermore that model systems, such as single crystal facet studies, will therefore lack the influence of

11

electronic effects that can contribute to structure sensitivity. That is, it is important to study a model system that is dynamic, can restructure, and in which the d-band energy or degree of electron (de-)localization can be examined (to also incorporate contributions from supports). Thus most importantly, we argue that structure sensitivity can currently only be fully understood in non-model catalysts.

In this work we have reported operando spectroscopy evidence for the effect of the Ni particle size on stability and reactivity of intermediates in CO_2 methanation over Ni, which serves to provide a mechanistic understanding of how to control the activity of this reaction. Furthermore, these results provide new found potential for the use of Ni in Fischer-Tropsch synthesis, which is often neglected as an industrially relevant FT catalyst due to the formation of highly toxic nickeltetracarbonyls which were not found to be present in our study with small Ni particles. We show decreasing CO adsorption strength with decreasing particle size. Thus, under the condition that the particles remain structurally stable, small Ni particles may find revived interest for Fischer-Tropsch synthesis as highly selective C_{5+} catalysts, on reducible supports[40,41]. The current operando spectroscopy study can be regarded as not only a major step forward in understanding the origin of Ni particle size effects in CO_2 hydrogenation and activation, but it also shines a light on the reactivity of intermediate CO with direct practical interest, for example in the Fischer-Tropsch synthesis of hydrocarbons. The analogous methodologies developed here also provide a fundamental insight in the performance-size relationship of CO_2 hydrogenation and, consequently may be applicable for studies of metal nanoparticle size effects in general.

1   # METHODS (800 WORDS)

2   **CATALYST SYNTHESIS.** Silica supported Ni nanoparticles were made by homogeneous deposition precipitation (HDP)

3   according to e.g. Ermakova et al[42]. The catalyst samples under investigation have varying Ni mean particle sizes, as listed in

4   Table 1.

5   **CATALYST CHARACTERIZATION.** Temperature programmed reduction (TPR) was performed in a Tristar II series

6   analyzer. The middle of the second reduction peak (Ni(II) to Ni (0)) was chosen as the reduction temperature for each

7   catalyst. Per these results, all reduction steps in this work were ramped at 5 °C min^{-1} to 600 °C (catalyst A), 550 °C (catalyst

8   B-G), and 500 °C (catalyst H), and held at these respective temperatures for 30 min. The oxidation states of the catalysts

9   after this procedure were examined by X-ray absorption spectroscopy, and were in a fully reduced condition prior to activity

10 experiments (see section 'Characterization Results' of the Supplementary information).

11 Materials for examination by scanning transmission electron microscopy (STEM) were dry dispersed onto a holey carbon

12 TEM grid. The catalyst samples were examined using BF- and HAADF-STEM imaging mode in an aberration corrected

13 JEOL ARM-200CF scanning transmission electron microscope (STEM) operating at 200 kV. This microscope was also

14 equipped with a Centurio silicon drift detector (SDD) system for X-ray energy dispersive spectroscopy (XEDS) analysis.

15 Furthermore, fresh, reduced and passivated, and spent samples were examined with transmission electron microscopy (TEM)

16 in an FEI Tecnai12 operated at 120 kV or in an FEI Tecnai20F operated at 200 kV. Samples were crushed and suspended in

17 ethanol under ultrasonic vibration. A drop of this suspension was brought onto a holey carbon film on a 300 mesh copper

18 grid. Metal particle sizes in Table 1 are surface-area averaged values (>100 particles). Particle size distributions were

19 determined by TEM for fresh, reduced and spent samples (see section 'Characterization Results' in the Supporting

20 information). X-ray diffraction (XRD) measurements of fresh, reduced (and re-oxidized), and spent samples were also

21 carried out in a Bruker D2 Phaser to determine crystallite size.

22 **OPERANDO FT-IR WITH ON-LINE PRODUCT ANALYSIS.** Operando Fourier transform infrared (FT-IR)

23 spectroscopy measurements were performed to study reactants, intermediates and products in CO_2 hydrogenation over Ni.

24 Product formation was followed by on-line gas chromatography. Time-resolved operando FT-IR spectra were recorded to

25 study the effect of different particle sizes on reaction intermediates and catalyst activity at different temperatures. The

26 operando FT-IR measurements were carried out using a Bruker Tensor 37 FT-IR spectrometer equipped with a DTGS

27 detector. Spectra were recorded every 30 s for each experiment. On-line product analysis was performed with an Interscience

28 custom-built Global Analyzer Solutions (G.A.S) Compact GC$_{4.0}$ gas chromatograph (GC) with a time resolution of around 10

s for lower hydrocarbons (methane, ethane, and ethene). The CO_2 hydrogenation experiments were carried out in a Specac High Temperature transmission IR reaction cell (as depicted in Figure S1). To this end, the catalyst powders were pressed into wafers of approximately 16mm in diameter, and around 0.1 mg thickness weighing between 10-15 mg. These self-supported catalyst wafers were created using a Specac Laboratory Pellet Press, a diaphragm vacuum pump and around 4 t of pressure. Before each reaction, each catalyst was reduced at a reduction temperature predetermined by TPR, and reduced in-situ with a 5 °C min^{-1} temperature ramp, and a 3 min hold in a 1:1, N_2:H_2 flow with a total of 25mL/min (both Linde, 4.9). After this in-situ reduction, the temperature of the reaction cell was brought to 100 °C, and the reactants were introduced through Bronkhorst EL-FLOW Mass Flow Controllers; CO_2 at 1.25mL min^{-1}, H_2 at 5 mL min^{-1} and N_2 to dilute at 6.25 mL min^{-1} for a total flow of 12.5 mL min^{-1}. In a temperature programmed reaction, the reactor was heated at a ramp of 5 °C min^{-1} to 400 °C, where eventually the temperature was held for 90 min. For each catalyst sample with differing metal dispersion, on-line activity data was collected with a time resolution of 30 s. Simultaneously, successive operando FT-IR spectra were also recorded with a time resolution of 30 s (see section 'FR-IR Studies of Catalyst Samples' in the Supplementary information).

OPERANDO QUICK-XAS WITH ON-LINE PRODUCT ANALYSIS. Operando X-ray absorption spectroscopy (and ex-situ characterization) with millisecond time resolution was performed at the SuperXAS beamline (X10DA) at the Swiss Light Source in transmission mode. The X-ray beam from the bending magnet was monochromatized with a Si(111) channel-cut crystal in the QuickXAS monochromator. The Si(111) crystal was rotated at a frequency of 10 Hz across the Ni K-edge, and the signals of the ionization chambers and the angular encoder were sampled at a frequency of 2 MHz. The edge energy was calibrated using a Ni foil. The measurements were performed in a custom-built operando reaction cell, which is described in more detail in the Supplementary information. Q-XAS data was evaluated using the JAQ Analyzes QEXAFS version 3.3.53 software and self-developed Matlab™ code was used for principal component analysis and subsequent clustering[43]. Least squares linear combination fitting of clustered spectra was performed using the Athena software[44]. Based on the signal to noise ratio the data was binned to an effective time resolution of 4 s. Further information about the Q-XAS data processing can be found in the Supplementary information.

REFERENCES

1.   United Nations. *Paris Agreement*. 1–6 (2015).

2.   McGlade, C. & Ekins, P. The geographical distribution of fossil fuels unused when limiting global warming to 2 °C. *Nature* **517,** 187–190 (2015).

3.   Ertl, G., Knözinger, H., Schüth, F. & Weitkamp, J. *Handbook of Heterogeneous Catalysis*. (Wiley VCH, Weinheim, 1997).

4.   Ertl, G. Reactions at surfaces: From atoms to complexity (nobel lecture). *Angew. Chem. Int. Ed.* **47,** 3524–3535 (2008).

5.   Somorjai, G. A. & Li, Y. *Introduction to Surface Chemistry and Catalysis*. (John Wiley & Sons, New York, 2010).

6.   Senderens, J.-B. & Sabatier, P. Nouvelles synthèses du méthane. *Compt. rend.* **82,** 514–516 (1902).

7.   Sabatier, P. & Senderens, J.-B. Hydrogénation directe des oxydes du carbone en présence de divers métaux divisés. *Compt. rend.* **134,** 689–691 (1903).

8.   Armstrong, R. C. *et al.* The frontiers of energy. *Nat. Energy* **1,** 1–8 (2016).

9.   Hull, J. F. *et al.* Reversible hydrogen storage using CO_2 and a proton-switchable iridium catalyst in aqueous media under mild temperatures and pressures. *Nat. Chem.* **4,** 383–388 (2012).

10.   Studt, F. *et al.* Discovery of a Ni-Ga catalyst for carbon dioxide reduction to methanol. *Nat. Chem.* **6,** 320–324 (2014).

11.   Schuchmann, K. & Muller, V. Direct and reversible hydrogenation of CO_2 to formate by a bacterial carbon dioxide reductase. *Science* 1382–1386 (2013).

12.   Rostrup-Nielsen, J. R., Pedersen, K. & Sehested, J. High temperature methanation - sintering and structure sensitivity. *Appl. Catal. A Gen.* **330,** 134–138 (2007).

13.   Silaghi, M., Comas-Vives, A. & Copéret, C. CO_2 activation on Ni/γ-Al_2O_3 catalysts by first-principles calculations: from ideal surfaces to supported nanoparticles. *ACS Catal.* **6,** 4501–4505 (2016).

14.   Kopyscinski, J., Schildhauer, T. J. & Biollaz, S. M. A. Production of synthetic natural gas (SNG) from coal and dry biomass – A technology review from 1950 to 2009. *Fuel* **89,** 1763–1783 (2010).

15.   Yan, Z., Ding, R., Song, L. & Qian, L. Mechanistic study of carbon dioxide reforming with methane over supported nickel catalysts. *Energy and Fuels* **12,** 1114–1120 (1998).

16.   Lewis, N. S. & Nocera, D. G. Powering the planet: Chemical challenges in solar energy utilization. *Proc. Natl. Acad. Sci.* **104,** 15729–15735 (2007).

17.   Steinfeld, A. Solar thermochemical production of hydrogen — a review. *Sol. Energy* **78,** 603–615 (2005).

18.   Centi, G. & Perathoner, S. Opportunities and prospects in the chemical recycling of carbon dioxide to fuels. *Catal. Today* **148,** 191–205 (2009).

19.   Tada, S., Shimizu, T., Kameyama, H., Haneda, T. & Kikuchi, R. Ni/CeO_2 catalysts with high CO_2 methanation activity and high CH4 selectivity at low temperatures. *Int. J. Hydrogen Energy* **37,** 5527–5531 (2012).

20.   van Santen, R. A. Complementary structure sensitive and insensitive catalytic relationships. *Acc. Chem. Res.* **42,** 57–66 (2009).

21.   van Hardeveld, R. & van Montfoort, A. The influence of crystallite size on the adsorption of molecular nitrogen on nickel, palladium and platinum. *Surf. Sci.* **4,** 396–430 (1966).

22.   Bezemer, G. L. *et al.* Cobalt particle size effects in the Fischer − Tropsch reaction studied with carbon nanofiber supported catalysts. *J. Am. Chem. Soc.* **128,** 3956–3964 (2006).

23.   Ren, J. *et al.* Insights into the mechanisms of CO_2 methanation on Ni(111) surfaces by density functional theory. *Appl. Surf. Sci.* **351,** 504–516 (2015).

24.   den Breejen, J. P. *et al.* On the origin of the cobalt particle size effects in Fischer - Tropsch catalysis. *J. Am. Chem. Soc.* **131,** 7197–7203 (2009).

25.   Heine, C., Lechner, B. A. J., Bluhm, H. & Salmeron, M. Recycling of CO_2: probing the chemical state of the Ni(111) surface during the methanation reaction with ambient-pressure X-Ray photoelectron spectroscopy. *J. Am. Chem. Soc.* **138,** 13246–13252 (2016).

26.   Czekaj, I., Loviat, F., Raimondi, F., Biollaz, S. & Wokaun, A. Characterization of surface processes at the Ni-based catalyst during the methanation of biomass-derived synthesis gas : X-ray photoelectron spectroscopy (XPS). *Appl. Catal. A Gen.* **329,** 68–78 (2007).

27.   Marwood, M., Doepper, R. & Renken, A. In-situ surface and gas phase analysis for kinetic studies under transient conditions - The catalytic hydrogenation of CO2. *Appl. Catal. A Gen.* **151,** 223–246 (1997).

28.   Tao, F. *et al.* Reaction-driven restructuring of Rh-Pd and Pt-Pd core-shell nanoparticles. *Science* 932–934 (2008).

29. Tao, F. *et al.* Break-up of stepped platinum catalyst surfaces by high CO coverage. *Science* **327,** 850–853 (2010).

30. Miao, D. *et al.* Water-gas shift reaction over platinum/strontium apatite catalysts. *Appl. Catal. B Environ.* **202,** 587–596 (2017).

31. Lamberti, C., Zecchina, A., Groppo, E. & Bordiga, S. Probing the surfaces of heterogeneous catalysts by in situ IR spectroscopy. *Chem. Soc. Rev.* **12,** 4951–5001 (2010).

32. Yardimci, D., Serna, P. & Gates, B. C. Surface-mediated synthesis of dimeric rhodium catalysts on MgO: Tracking changes in the nuclearity and ligand environment of the catalytically active sites by X-ray absorption and infrared spectroscopies. *Chem. - A Eur. J.* **19,** 1235–1245 (2013).

33. Kalz, K. F. *et al.* Future challenges in heterogeneous catalysis: understanding catalysts under dynamic reaction conditions. *ChemCatChem* 1–14 (2016).

34. Camputano, J. C. & Greenler, R. G. The adsorption sites of CO on Ni(111) as determined by infrared reflection - absorption spectroscopy. *Surf. Sci.* **83,** 301–312 (1979).

35. Trenary, M., Uram, K. J. & Yates, J. T. An infrared reflection-absorption study of CO chemisorbed on clean and sulfided Ni(111) - evidence for local surface interactions. *Surf. Sci.* **157,** 512–538 (1985).

36. Layman, K. A. & Bussell, M. E. Infrared spectroscopic investigation of CO adsorption on silica-supported nickel phosphide catalysts. *J. Phys. Chem. B* **108,** 10930–10941 (2004).

37. Courtois, M. & Teichner, S. J. Infrared studies of CO, O_2 and CO_2 gases and their interaction products, chemically adsorbed on nickel oxide. *J. Catal.* **135,** 121–135 (1962).

38. van Bokhoven, J. A. & Lamberti, C. *X-Ray Absorption and X-Ray Emission Spectroscopy: Theory and Applications*. (John Wiley & Sons, New York, 2016).

39. Bordiga, S., Groppo, E., Agostini, G., Van Bokhoven, J. A. & Lamberti, C. Reactivity of surface species in heterogeneous catalysts probed by in situ X-ray absorption techniques. *Chem. Rev.* **113,** 1736–1850 (2013).

40. Enger, B. C. & Holmen, A. Nickel and Fischer-Tropsch Synthesis Nickel and Fischer-Tropsch. **4940,** (2016).

41. Munnik, P., Velthoen, M. E. Z., de Jongh, P. E., De Jong, K. P. & Gommes, C. J. Nanoparticle growth in supported nickel catalysts during methanation reaction-larger is better. *Angew. Chem. - Int. Ed.* **53,** 9493–9497 (2014).

42. Ermakova, M. A. & Ermakov, D. Y. High-loaded nickel-silica catalysts for hydrogenation, prepared by sol-gel route: structure and catalytic behavior. *Appl. Catal. A Gen.* **245,** 277–288 (2003).

43. Liu, Y. *et al.* TXM-Wizard: A program for advanced data collection and evaluation in full-field transmission X-ray microscopy. *J. Synchrotron Radiat.* **19,** 281–287 (2012).

44. Ravel, B. & Newville, M. ATHENA, ARTEMIS, HEPHAESTUS: Data analysis for X-ray absorption spectroscopy using IFEFFIT. *J. Synchrotron Radiat.* **12,** 537–541 (2005).

45. Chumakova, A. V. *et al.* Periodic order and defects in Ni-based inverse opal-like crystals on the mesoscopic and atomic scale. *Phys. Rev. B - Condens. Matter Mater. Phys.* **90,** 1–9 (2014).

46. Frenkel, A. I., Hills, C. W. & Nuzzo, R. G. A view from the inside: Complexity in the atomic scale ordering of supported metal nanoparticles. *J. Phys. Chem. B* **105,** 12689–12703 (2001).

47. Chukin, G. D. & Malevich, V. I. Infrared spectra of silica. *Zhurnal Prikl. Spektrosk.* **26,** 223–229 (1977).

48. Socrates, G. *Infrared and Raman Characteristic Group Frequencies*. (Wiley, 2001).

49. Erley, W., Wagner, H. & Ibach, H. Adsorption sites and long range order - vibrational spectra for CO on Ni(111). *Surf. Sci.* **80,** 612–619 (1979).

50. Erley, W. & Wagner, H. Thermal decomposition of CO on a stepped Ni surface. *Surf. Sci.* **74,** 333–341 (1978).

COMPETING FINANCIAL INTERESTS

The authors declare no competing financial interests.
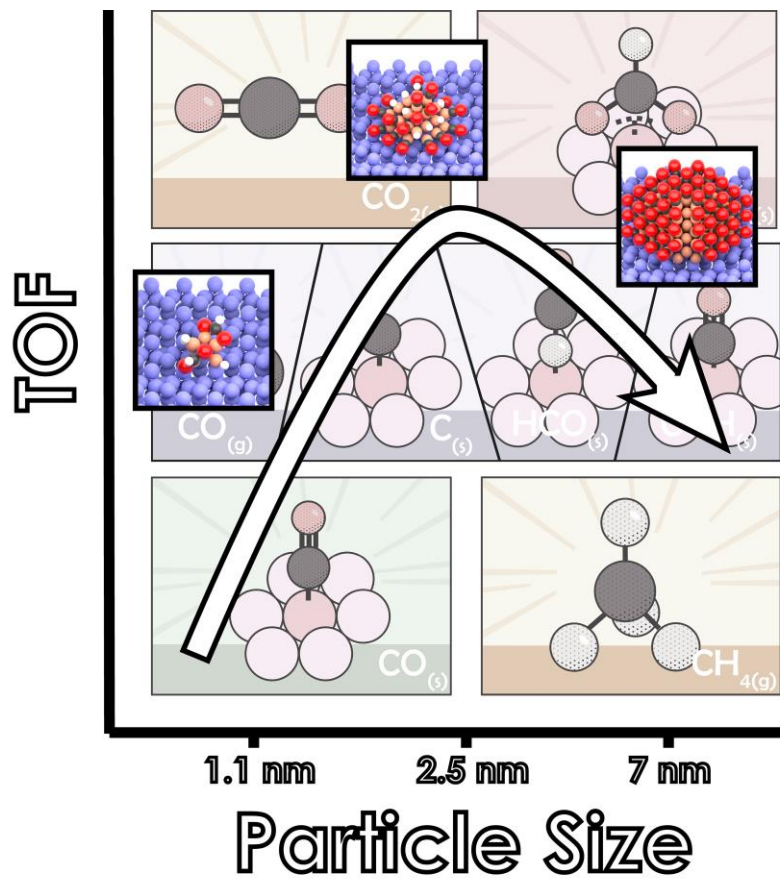
TOC Figure

Table 1. Characteristics of the set of well-defined Ni/SiO$_2$ catalysts (A-H), listing their Ni loadings, and Ni particle sizes after reduction, and of spent catalysts as determined by TEM, HAADF-STEM, XRD, and XAS.;

Sample[a]	Ni loading (wt%)	NiO TEM particle size spent (nm)[b]	Ni HAADF-STEM particle size after reduction (nm)[c]	Ni XAS coordination number (particle size) after reduction[45,46 e]	NiO XRD particle size after reduction (nm)[d]
A	1.0	1.1 ±0.4	1.82 ±0.75	6.4 ±1.2 (1 nm)	1.0 ±0.9
B	5.0	1.6 ±0.3	1.42 ±0.41	7.3 ±1.2 (2 nm)	1.2 ±0.6
C	4.7	1.6 ±0.7	1.23 ±0.48	7.1 ±1.5 (1.5 nm)	1.2 ±1.0
D	6.7	2.5 ±0.7	2.04 ±0.78	7.6 ±1.3 (2 nm)	0.9 ±0.2
E	1.7	2.6 ±0.5	1.36 ±0.40	5.8 ±3.1 (1 nm)	1.9 ±41
F	11.8	3.5 ±0.6	2.10 ±1.09	7.3 ±2.1 (2 nm)	2.3 ±1.2
G	19.5	5.0 ±1.4	4.43 ±2.39	7.4 ±1.3 (2 nm)	4.2 ±1.6
H	60.0	6.9 ±1.9	6.08 ±1.93	8.8 ±1.1 (6 nm)	5.2 ±2.6

[a] Arbitrary codes denoted from smallest (A) to largest (H) catalyst particle sizes determined as spent particle sizes from TEM, [b] Average of at least 100 particles per sample, of spent samples, [c] Particle size distributions determined after reduction step (and re-oxidation by exposure to air) of at least 120 nanoparticles, see Supplementary information for additional details on HAADF-STEM analysis, [d] Full-width at half-maximum (FWHM) X-ray diffraction analysis of catalysts after reduction step, and re-oxidation by exposure to air, [e] XAS particle sizes (in brackets) determined from coordination numbers ex-situ for particles after the respective reduction step (fit of first coordination shell)[46,44]